RESEARCH ARTICLE-CHEMISTRY

Photocatalytic Performance of Organically Templated Cr-Doped Co$_3$O$_4$ in Remediation of Industrial Wastewater: Effect of Order–Disorder in the Lattice

Nasser H. Shalaby[1]

Abstract

In photocatalysis, the optical properties and surface parameters significantly affect the catalytic performance. To engineer the optical properties and textural structure, Cr and *p*-phenylene diamine (PDA) were utilized as dopant and textural structure regulator, respectively. A series of Cr-doped Co$_3$O$_4$ with dopant percentages of 0, 1, 3, and 5, templated PDA at a fixed ratio of 5%, and another un-templated sample with a dopant ratio of 5% were prepared. The co-precipitation method was applied in swift and innovative procedures, where a calculated amount of NaOH was used as a precipitant. The optical properties, dopant concentration quenching, and surface parameters are strongly affected by the order–disorder in the lattice and dopant concentration. The lattice regularity affects the optical properties and the surface parameters along with the dopant concentration. The photocatalysts were evaluated in the disposal of organic pollutants in a representative sample of wastewater collected from different industrial activities. The function of another function was applied to monitor the pollutants' disposal, taking the total organic carbon (TOC) as a function of the pollutants' concentration and the photometric absorbance as a function of the TOC. The kinetic investigation exhibited the significant role of the pore system on the reaction rate.

Keywords Photocatalytic performance · Doping · Cobalt oxide · Wastewater remediation · Lattice regularity

1 Introduction

Water, energy, and the environment are the current and future challenges worldwide. Water is the main requirement for all human activities, animals, plants, and micro-organisms [1]. The quality and specifications of water determine its suitability for use for diverse purposes. The rapid pace of industrial development and its by-products, which include smoke, hazardous waste, and poisonous gas emissions, have a severe impact on the environment [2]. Contamination with organic compounds is one of the most prevalent contaminants in wastewater [2, 3]. The detergent, textile, food processing, ship maintenance, oil and gas sectors, etc., are the important assets that release organic pollutants that end up in the water [4]. The contamination with a low amount of organic pollutants causes the water to collect distinctive colors, which prevents daylight from penetrating and disrupts

aquatic lifestyles and the ecology; its disposal has emerged as one of the most challenging situations [5]. Therefore, wastewater treatment and recycling are principal issues, and researchers are working to create low-cost, effective generation technology. Different physical, chemical, and biological techniques have been used to treat wastewater. One of the most promising technologies for wastewater remediation is the advanced oxidation process [6]. Heterogeneous photocatalysis is a potential technique among many advanced oxidation processes that can be utilized to degrade different organic contaminants in wastewater [7]. Over the past two decades, great attention has been paid to the reactions that occur at the irradiated surface of semiconductor metal oxides and sulfides [5, 8]. The semiconductors with moderate bandgap energy of 1.7–3.32 eV between their valence and conduction bands are TiO$_2$, ZnO, CuO, CdS, ZnS, Co$_3$O$_4$, and WO$_3$. The wide band energy gap restricts the catalyst's viability and reasonability for usage in industrial applications because UV makes up approximately 4% of solar radiation [9].

Because of its magnetic, electrical, and catalytic capabilities, Co$_3$O$_4$ has attracted the attention of many researchers.

✉ Nasser H. Shalaby
chem.shalaby@gmail.com

1 Egyptian Petroleum Research Institute, 1 Ahmed El-Zomor St., Nasr City, Cairo 11727, Egypt

⚛ 🍃 Springer

Several research papers have been published on the doping of cobalt oxide with various transition metals such as Fe, B, Cr, and Ag for its use in supercapacitors, potential electrodes, catalytic and photocatalytic oxidation processes [5, 10–14]. Also, the effect of dopant concentration on catalytic activity in Cr-doped Co_3O_4 was reported without discussing the effect of lattice regularity on the optical properties and dopant concentration quenching [15]. The current work aims to study the effect of the dopant ratio along with the order–disorder in the lattice on the optical properties, dopant concentration quenching, surface analysis, and consequently photocatalytic performance. The as-prepared photocatalysts were evaluated in the disposal of different organic pollutants from a representative sample of different industrial wastewater.

2 Experimental

2.1 Materials

All the used chemicals, chromium chloride hexahydrate ($\geq$ 98.0%), cobalt nitrate hexahydrate (99.999%), sodium hydroxide ($\geq$ 98%, pellets, anhydrous), Triton X-100 surfactant (laboratory grade), and *p*-phenylene diamine (PDA) (99.5%), purchased from Sigma-Aldrich and used without further treatment. Samples of organic pollutants contaminated wastewater were collected from different companies, such as companies producing detergents, foods, pesticides, and textiles. The collected samples were mixed in equal volumes to be a representative sample. The representative sample was let overnight for decantation.

2.2 Preparation of Catalytic Materials

Composites of Co_3O_4 and Cr_2O_3 at different ratios templated with PDA at a fixed percent ratio of 5% were prepared. The metal precursors, $Co(NO_3)_2 \cdot 6H_2O$ and $CrCl_3 \cdot 6H_2O$, were dissolved in demineralized water before adding PDA at a rate of 5% (based on the expected metal oxide). Gelatinous mixed hydroxides were co-precipitated by adding a precisely calculated amount of NaOH equivalent to the Cl^- and NO_3^- portion-wise with vigorous stirring, Eq. (1).
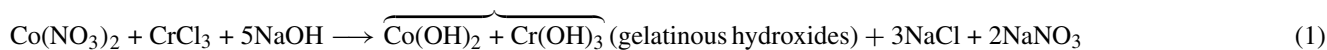
clean porcelain crucible to put in a programmed muffle with multi-stage heating. The first heating stage was adjusted at 120 °C for 3 h, followed by the second stage in which the template was removed under controlled heating by raising the temperature with a ramp of 5 °C min^{-1} and held for 2 h at 600 °C to obtain porous Co-Cr mixed oxides. The same procedures were repeated to prepare a series of Cr-doped Co_3O_4 with Cr_2O_3 percentages of 0, 1, 3, and 5. The materials obtained were designated as $(CoO)_T$, $(1\%Cr_2O_3: CoO)_T$, $(3\%Cr_2O_3: CoO)_T$, and $(5\%Cr_2O_3: CoO)_T$, respectively. A sample of Cr-doped Co_3O_4 with a dopant ratio of 5% without the template was prepared. The sample was denoted as $(5\%Cr_2O_3: CoO)_{WT}$.

2.3 Photocatalytic Evaluation

The as-prepared catalytic materials were employed in the photocatalytic degradation of industrial organic pollutants. In the photocatalytic performance test, a cylindrical batch-type quartz reactor was used. Magnetic stirring was utilized to keep the catalyst in suspension. In all experiments, the water-dissolved oxygen was compensated by aeration through bubbling using a small blower. A 300 W high-pressure mercury lamp was utilized to provide visible light (Yaming Company, Shanghai). Before each run, the lamp was turned on and warmed up for 10 min to ensure a constant light output. For a homogenous dispersion of the organic phase, a non-ionic surfactant, namely Triton X-100, was added in a dose of $0.5\,g\,L^{-1}$ with vigorous stirring to obtain a stable emulsion. For spectrophotometric monitoring for the photodegradation of organic contaminants, the total organic carbon (TOC) was taken as a function in the concentration of organic contaminants and the photometric absorbance as a function in the TOC, viz., a function of another function is applied. The calibration curve was obtained by drawing six samples from a prepared emulsion and diluting them at different concentrations to cover the range of the samples under study. The total organic carbon (TOC) of the drawn samples was standardized using analytikjena Multi N/C 2100s, Germany. The TOC is plotted against the average value of two readings of the absorbance of each datum point at the obtained λ_{max} (325 nm) using a Shimadzu 1603 spectrophotometer, Fig. 1. Another stock of the emulsified contaminated water with pollutants'

$$Co(NO_3)_2 + CrCl_3 + 5NaOH \longrightarrow \overbrace{Co(OH)_2 + Cr(OH)_3} \text{ (gelatinous hydroxides)} + 3NaCl + 2NaNO_3 \qquad (1)$$

The templated mixed hydroxides were stirred for 48 h and recovered by filtration, then washed with demineralized water several times to ensure the complete removal of NaCl and NaNO_3. The clean gelatinous precipitate was put in a

initial concentration of 150 ppm (TOC) was prepared by dilution with distilled water for catalytic performance evaluation.

In the range of 0.5–1.5 g L^{-1}, the influence of catalyst dosage on catalytic performance was examined. During both
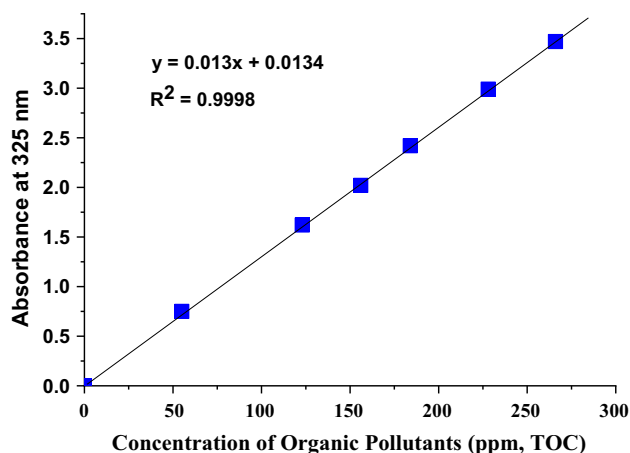
Fig. 1 Photometric calibration curve of the organic pollutants at λ_{max} 325 nm

the dark sorption and visible light irradiation periods, the chosen catalyst dose was distributed in 100 mL of the emulsified pollutants. In each experiment, aliquots (10 mL) of the sample were taken every hour and filtered through a sintered glass filter with a 0.2 μm Millipore disk. The average value of each datum point was recorded after each run was done twice. The efficiency of the catalytic photodegradation process was estimated using Eq. (2):

$$Degradation(\%) = \frac{C_o - C_t}{C_o} \times 100 \qquad (2)$$

where C_o is the initial concentration of contaminated organic pollutants and C_t is the detected concentration at a time "t" expressed in ppm of TOC.

2.4 Characterization Procedures

The constitutional composition and the role of the template and the dopant were investigated using SEM imaging with EDX field emission, XRD patterns, BET surface analysis, and XP spectra. The SEM images and EDX analysis were examined on a Zeiss Sigma 300 vp Field Emission electron microscope. An X-ray diffractometer, PANalytical model X, pert PRO, with a Cu K radiation (k = 1.5418 Å) and a scanning rate of 0.3 min^{-1} was used for the XRD analysis. Nitrogen adsorption–desorption isotherms at 196 °C were used to characterize the textural analysis of the catalytic systems utilizing the NOVA 3200, USA. The samples were pre-treated for surface degassing for 2 h under vacuum (104 Torr) at 150 °C. The surface areas (S_{BET}) were calculated using the BET equation from the adsorption isotherms branch. The Barrett, Joyner, and Halenda (BJH) method was applied to estimate the pore size distribution from the isotherms desorption branch. The X-ray photoelectron spectroscopy (XPS) data were collected on K-ALPHA (Thermo

Fisher Scientific, USA) using monochromatic X-ray Al K-alpha radiation with a spot size of 400 μm at a pressure of 10–9 mbar and a full-spectrum pass energy of 200 eV and a narrow-spectrum pass energy of 50 eV.

The diffusional reflectance (R) and photoluminescence spectra (PL) were recorded to investigate the optical properties. The diffusional reflectance spectra were acquired using a Jasco V-750 spectrophotometer in the wavelength range of 200–800 nm. A spectrofluorometer (JASCO FP-6500) with an excitation wavelength of 300 nm was used to record the photoluminescence (PL) characteristics of the samples at room temperature.

3 Results and Discussion

The current study focuses on three main points: (1) the design of a photocatalyst with good activity in the visible region through doping or, in other words, hybridization between the photoactive materials where the energy gap is diminished; on the other hand, the tuning of the textural structure using a suitable pore regulator, (2) the correlation between the order–disorder in the lattice, dopant concentration, dopant concentration quenching, and photocatalytic activity; and (3) the use of the as-prepared catalyst in the photodegradation of organic pollutants in a representative sample of industrial wastewater collected from the wastewater of some companies with different activities.

3.1 Constitutional Examination

In this study, Cr-doped Co_3O_4 with different Cr: Co ratios were synthesized via the co-precipitation method. To avoid the problem that may result from the use of ammonium hydroxide as a precipitant, which leads to the dissolution of some of the objective materials [16], sodium hydroxide equivalent to the acid radicals of the precursors (NO_3^- and Cl^-) was used as a precipitant in the presence of p-phenylene diamine as a pore regulator. The constituent properties of the as-obtained materials were investigated by XRD, XPS, SEM, and BET surface analysis.

The XRD patterns of $(5\%Cr_2O_3: CoO)_T$ and $(5\%Cr_2O_3: CoO)_{WT}$ are displayed in Fig. 2, using JCPDS No. 80-1535, space group Fd3m. From the patterns of both samples, it can be seen that both samples have the same crystal phases with a high degree of crystallinity, the same lattice planes, and crystallite sizes, revealing that the crystal growth is not affected by the existence of the template. The crystallite size was calculated using the Scherrer equation [17] at the main peak centered at 36.75 °C:

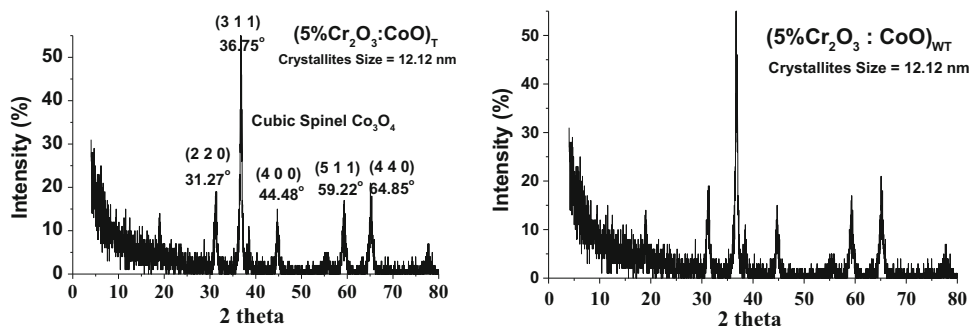$$\tau = \frac{K\lambda}{\beta \cos\theta} \qquad (3)$$

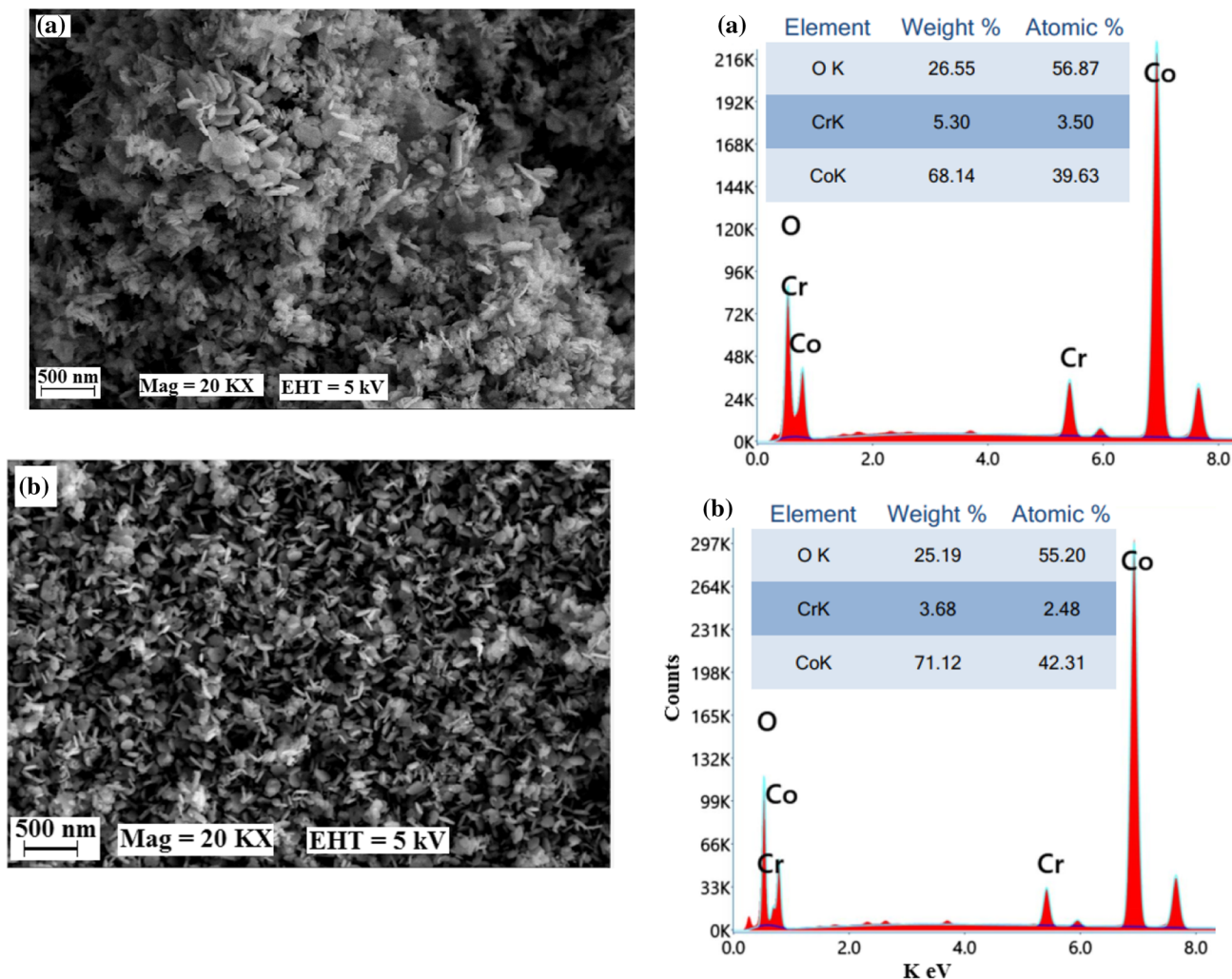**Fig. 2** XRD patterns of $(5\%Cr_2O_3: CoO)_T$ and $(5\%Cr_2O_3: CoO)_{WT}$

Fig. 3 SEM image and EDX spectra of: **a** $(5\%Cr_2O_3: CoO)_{WT}$; and **b** $(5\%Cr_2O_3: CoO)_T$

where K is dimensionless in shape factor with a value of about 0.9, λ is the X-ray wavelength (= 1.5418), β is the line broadening at half maximum intensity (FWHM) in radians, θ is the Bragg's angle, and "τ" is the average size of the ordered crystalline domains, which may be smaller or equal to the particle size. As shown in Fig. 2, the position and relative intensities of the peaks are compatible with cubic spinel

Co_3O_4 phases, implying that Co_3O_4 formation is preferred [18]. The peaks at 31.27°, 36.75°, 44.48°, 59.22°, and 64.85° are assigned to (220), (311), (400), (511), and (440) planes of the cubic spinel Co_3O_4 (cf., the SEM images). The absence of Cr characteristic peaks suggests that chromium ions have been well incorporated into the Co lattice with good dispersion.

Table 1 The XPS data of $(5\%Cr_2O_3: CoO)_T$

Name	Peak BE	FWHM eV	Atomic%
Co2p	781.31	4.62	33.9
O1s	531.19	3.58	62.66
Cr2p	577.41	4.85	3.44
C1s	286.01	4.09	0

The SEM images and EDX spectra of $(5\%Cr_2O_3: CoO)_{WT}$ and $(5\%Cr_2O_3: CoO)_T$ are depicted in Fig. 3. The lattice of $(5\%Cr_2O_3: CoO)_T$ appears more ordered than that of $(5\%Cr_2O_3: CoO)_{WT}$, revealing the role of PDA as a textural structure regulator. In the SEM image of $(5\%Cr_2O_3: CoO)_T$, Co_3O_4 sharpened nanoparticles with sizes between 20 and 40 nm have been observed. Although $(5\%Cr_2O_3: CoO)_{WT}$ has the same crystallite size as that of $(5\%Cr_2O_3: CoO)_T$, as detected from XRD patterns, its SEM image depicts bigger nanoparticles in the range of 80–120 nm. The corresponding EDX spectra exhibit the existence of Cr, Co, and O with a Co: O atomic ratio of ~ 3:4, confirming the formation of Co_3O_4 in good agreement with XRD spectra.

As catalysis is a surface phenomenon, the surface chemistry and properties determine the catalytic performance of catalytic materials. The surface chemistry and the chemical states of the elements located on the surface were investigated from XP- spectra. As shown in Table 1, the negligible content of C reveals the low surface contamination and the accuracy of quantitative measurements. Figure 4 displays the survey spectrum and the deconvolution spectra of Co, Cr, and O on the surface of $(5\%Cr_2O_3: CoO)_T$. The deconvolution of the Co2P and Cr2P spectrum indicates a multi-splitting accompanied by the characteristic satellites suggesting the existence of different oxidation states [19]. The deconvolution of Co2P depicts an intense peak centered at 780.96 eV assigned to 2P3/2 with doublet splitting at 779.78 eV and 780.9 eV assigned to 2P3/2 of $CoCr_2O_4$ and Co_3O_4, respectively.

Also, an intensive broad peak is observed at 795 eV that fits with 2P1/2 with doublet splitting at 794.3 eV and 796 eV assigned to 2P1/2 of $CoCr_2O_4$ and Co_3O_4, respectively [19]. The deviation in the values of BE of the characteristic peaks (from the standard values of pristine materials) is due to the work function of the material, which is an onto function, viz., a function in the material identity, Eq. (4):

$$BE = E_{photon} - (E_{kinetic} + W_f) \qquad (4)$$

BE is the binding energy, which equals the energy required to free an electron from the nucleus attraction force, E_{photon} is the photon energy of the applied X-ray, $E_{kinetic}$ is the kinetic energy of the ejected electron, and W_f is the work function,

which is a characteristic value for the material surface and defined as the minimum energy required to release an electron (in the vacuum) from a solid to be loosely on the material surface with zero kinetic energy. The BE of Co2P in Cr-Co compound oxide is lower than in the case of Co_3O_4, which runs in harmony with bandgap results.

For Cr2P, the spectrum deconvolution exhibits that Cr^{+3} is the predominant oxidation state. The obtained spectra consist of two main intensive peaks at 576.1 eV and 585.7 eV, corresponding to Cr2P3/2 and Cr2P1/2, respectively. The doublet splitting is due to the existence of Cr^{+3} with a higher population and Cr^{+6}. The intimal four peaks observed at 576 eV, 578 eV, 585 eV, and 587.4 eV are assigned to Cr^{+3}2P3/2, Cr^{+6}2P3/2, Cr^{+3}2P1/2, and Cr^{+6}2P1/2, respectively [20].

For O1S, the intense peak at 529.93 eV is assigned to the 'O^{-2}' ions of the lattice oxide. Another broad peak with lower intensity at 530.92 eV is attributed to the subsurface oxygen ions with lower electron density than O^{-2} and described as O^- species [21]. This may be linked to sites with a lower oxygen ion coordination number and a higher M–O bond covalence than conventional sites. This could be linked to the various oxidation states of Co and Cr (Co^{+2}, Co^{+3}, Cr^{+3}, and Cr^{+6}), which lead to an increase in the concentration of O^- species. The surface oxygen vacancy (SOV) has been observed to induce sub-bands between the valence band (VB) and the conduction band (CB), which has a significant impact on the PL properties [8].

The surface parameters derived from adsorption–desorption isotherms are given in Table 2, including specific surface areas (S_{BET}, m^2/g), pore volumes (V_p, cc g^{-1}) estimated at 0.95 p/p^o, and the average pore diameter (D_p^{cp}) assuming a cylindrical pore (cp) model derived from PSD curves are depicted in Fig. 5. As shown in Table 2, textural remodeling of CoO using the PDA and Cr-dopant can result in a significant increase in the surface area accompanied by a diminishing in pore parameters. The PDA molecule, as a *symmetric* bidentate ligand, and Cr-dopant engineer the pore system to give *unimodal* PSD curves with a narrower pore system. For all samples, the PDS curves represent a main peak of the most frequent hydraulic radius, ranging from 7.2 to 13.3 nm. The textural tuning and individual role of Cr-dopant and PDA template can be represented by comparing the PSD curve of $(CoO)_T$ with $(5\%Cr_2O_3: CoO)_T$ and $(5\%Cr_2O_3:CoO)_{WT}$.

It is obvious that Cr-dopant creates a narrower pore system and evolves a much larger interval surface area. The S_{BET} jumps from 61.4 m^2/g for $(CoO)_T$ with polymodal PSD curve to 125.7 m^2/g for $(5\%Cr_2O_3: CoO)_T$ with unimodal PSD curve and diminished pore parameters. Also, the PDA could lead to marked increases in surface area from 98.6 m^{2}g^{-1} for $(5\%Cr_2O_3: CoO)_{WT}$ to 125.7 m^{2}g^{-1} for $(5\%Cr_2O_3: CoO)_T$. These findings run in harmony with SEM images in Fig. 3 and postulate the formation of pore structure involving Co, Cr and amine [22], Fig. 6.
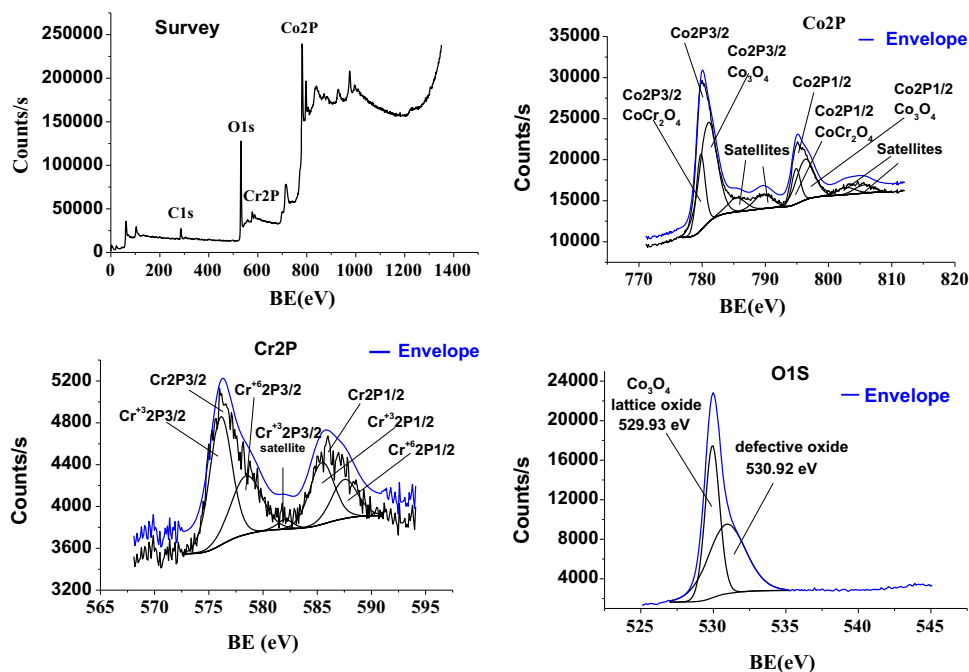
Fig. 4 XP-spectrum of $(5\%Cr_2O_3: CoO)_T$ and its constituent metallic species

Table 2 Values of the surface analysis of the as-prepared photocatalysts

Item	$(CoO)_T$	$(1\%Cr_2O_3:CoO)_T$	$(3\%Cr_2O_3:CoO)_T$	$(5\%Cr_2O_3:CoO)_T$	$(5\%Cr_2O_3:CoO)_{WT}$
D_P^{CP} (nm)	13.2	9.41	8.11	7.52	7.92
$V_P^{0.95}$ (cm^3 g^{-1})	3.95	2.91	2.62	2.42	2.54
S_{BET} (m^2 g^{-1})	61.4	88.3	102.4	125.7	98.6

The bandgap energy (E_g) and PL spectra of a semiconductor define the energy required to generate e$^-$/h* pairs, the efficiency of trapping, migration, and transition of charge carriers, as well as the fate of the e–h* pairs, which gives a prediction of the photocatalytic performance. Figure 7 shows the Tauc plot and PL spectra for the as-prepared materials. From the figure, it is noticed that there is a significant effect of the template and the dopant on the E_g value and the PL spectra. This could be attributed to the influence of the intermediary energy levels between the VB and CB, as the exponential optical absorption edge and E_g are controlled by the degree of structural order–disorder in the lattice, dopant concentration, and crystal size [23]. Also, all materials have two bandgaps that are most probably related to $O_2^- \rightarrow Co^{+3}/Cr^{+6}$ charge transitions for the lower transition bandgap (the main peak) and $O_2^- \rightarrow Co^{+2}/Cr^{+3}$ for the higher bandgap [15]. The decrease in the bandgap value with increasing dopant concentration could be attributed to the induction of sub-bands between the VB and the CB, which leads to a change in the distribution of the electron trap within the forbidden bandgap, as discussed in XP spectra. The increase in the broadness of the lower bandgap with

an increase in the dopant concentration has been attributed to the shifting to lower values due to the increase in created defects during the crystals' growth process [24]. By comparing the Tauc plot of $(5\% Cr_2O_3: CoO)_T$ and $(5\% Cr_2O_3: CoO)_{WT}$, the effect of the regularity of the crystal lattice on E_g is evident.

For PL spectra, the PL emission intensity is significantly influenced by: (1) the dopant concentration and (2) the order–disorder in the lattice. To show the doping material's effect, the other agent must be fixed. So, using $(CoO)_T$ as reference material, $(1\% Cr_2O_3: CoO)_T$, $(3\% Cr_2O_3: CoO)_T$, and $(5\% Cr_2O_3: CoO)_T$ were put in comparison with each other. It is obvious that the PL intensity for $(1\%Cr_2O_3:CoO)_T$ is decreased, compared to $(CoO)_T$, to come back to increase with the increase in the dopant concentration up to 3%. As the concentration is increased further, the PL intensity begins to decrease. This suggests that the dopant concentration of 3% is the critical value; beyond it, the phenomenon of concentration quenching occurs [25]. The primary source of concentration quenching is the cross-relaxation mechanism, which is the non-radiative energy transfer between the dopant activator ions through different interactions. The effect of
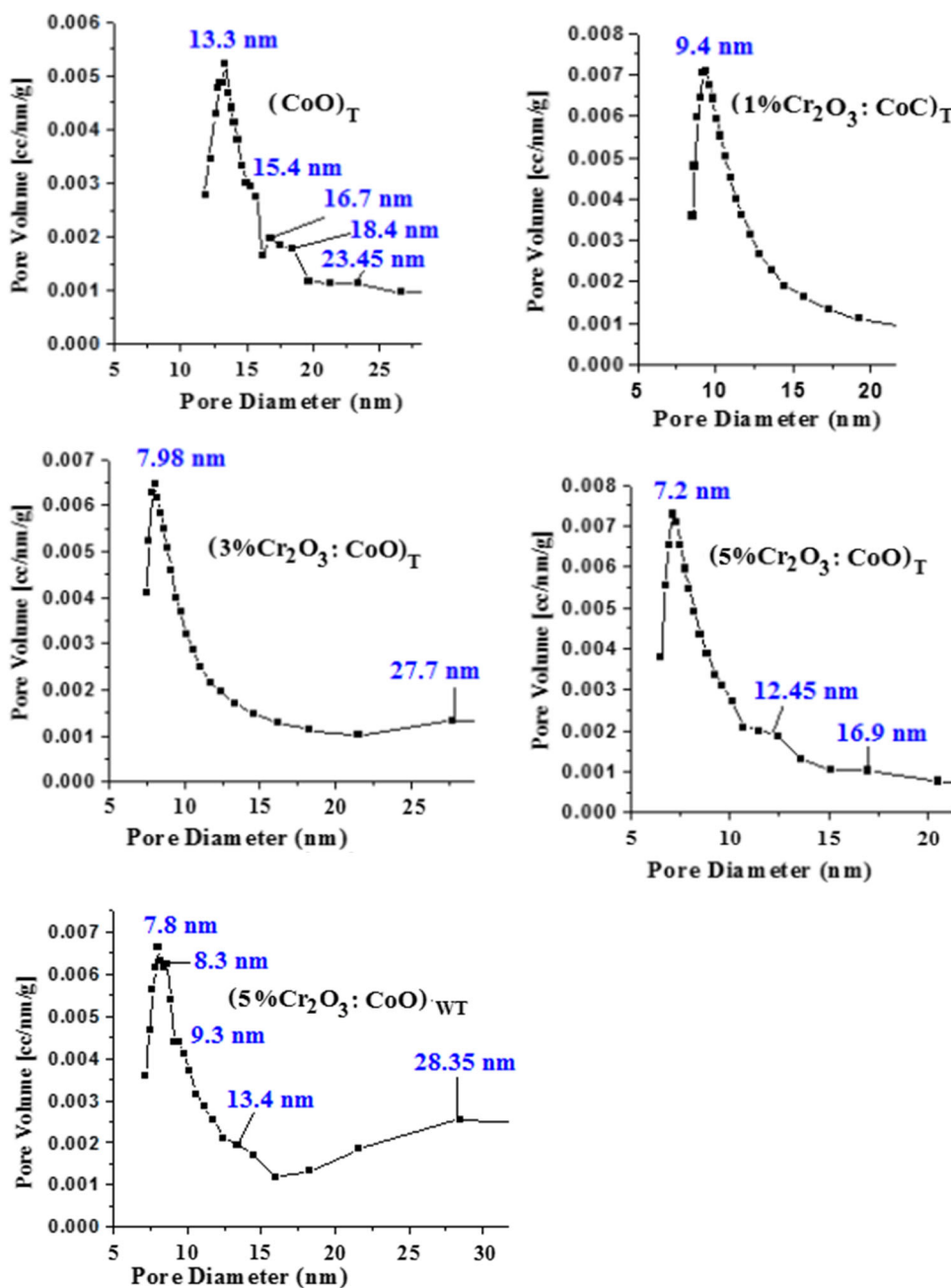
Fig. 5 PSD of the as-prepared photocatalysts

lattice regularity on the PL spectra is demonstrated by comparing the spectrum of $(5\%Cr_2O_3: CoO)_T$ and $(5\%Cr_2O_3: CoO)_{WT}$. Although both samples have the same dopant concentration, $(5\%Cr_2O_3: CoO)_T$ shows a lower PL intensity than $(5\%Cr_2O_3: CoO)_{WT}$, revealing that the order–disorder in the lattice has a significant effect on PL spectra and that the dopant concentration is not the only factor in determining the dopant concentration quenching. This result is consistent with and confirms Dexter's equation:
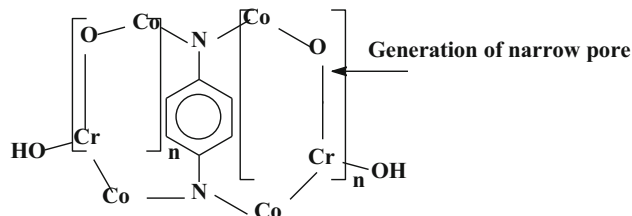

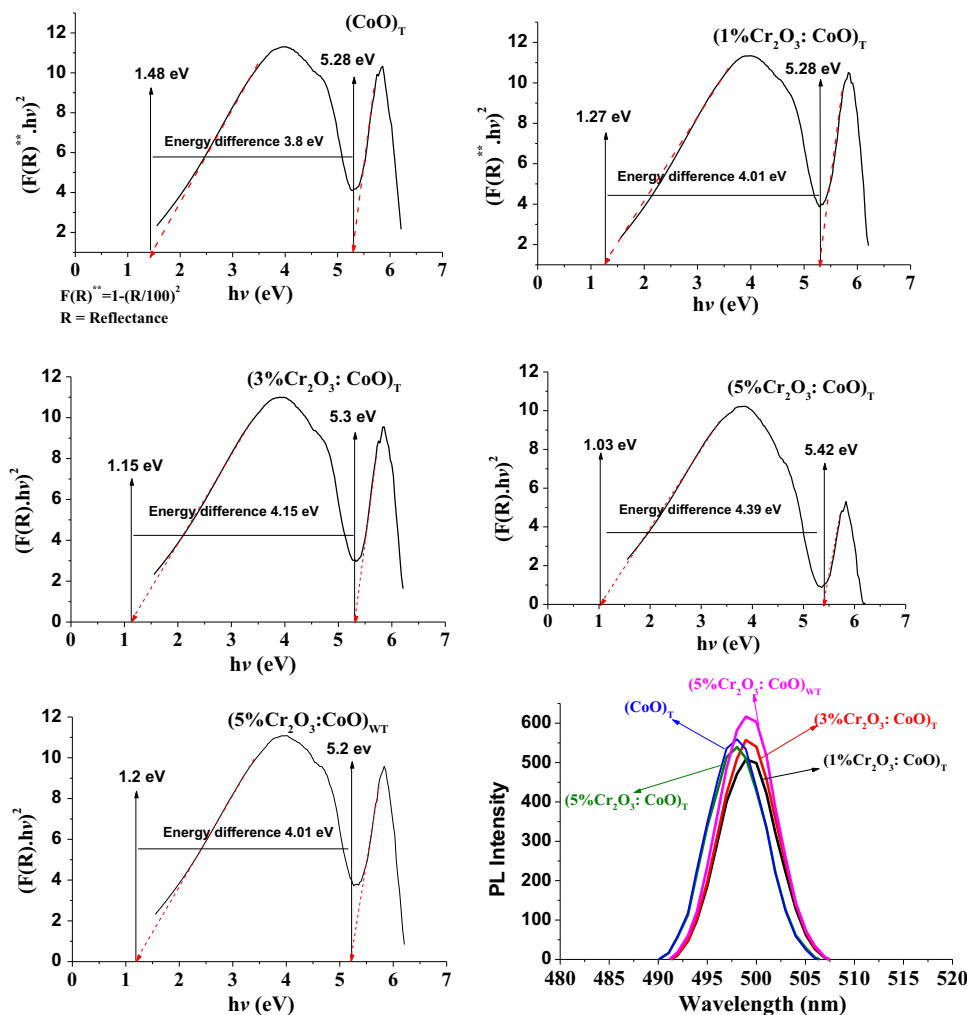**Fig. 6** The probable formation of pore structure involving Co, Cr and the amine

Fig. 7 Band gap energy calculated from Tauc plot and PL spectra of the as-prepared photocatalysts

$$\frac{1}{x} = \frac{K}{1 + \beta(x)^{Q/a}} \tag{5}$$

$1/x$ is the PL intensity per quencher concentration; Q is the exchange interaction, whereas K and β are constants characteristic of a given lattice.

3.2 Photocatalytic Performance

After the textural analysis, surface chemistry, and optical properties are provided, the as-prepared materials are employed and evaluated in the photodegradation of organic contaminants in industrial wastewater at ambient temperature. In each experiment, 100 mL of emulsified organic pollutants in wastewater (150 ppm as TOC) were vigorously stirred with the chosen catalyst dose in a dark period for 1 h to attain the pre-equilibrium sorption of the substrate on the catalyst surface. Then, the disposal of the organic contaminants was continued under visible irradiation to assess each material's rate of photodegradation of the organic pollutants.

In the dark period, the optical properties have no role in removing the pollutants, only the textural structure and the active sites intensity determine the sorptivity of the catalytic material. So, in this period, as shown in Fig. 8, the amount of the organic pollutants sorbed by the materials slightly increased as the catalyst dose was increased from 0.5 to 1 g L^{-1}. This can be attributed to the increase in the active sites as the catalyst dose increased. Figure 8 shows that there was no increase in pollutant sorption as the catalyst dose was raised to 1.5 g L^{-1}, indicating that the sorption equilibrium had been reached and no additional sorption was possible.

Generally, at different catalyst doses, $(5\%Cr_2O_3: CoO)_T$ has the highest sorptivity. Precisely, the maximum removal of the organic pollutants with a percentage of 58.8% was achieved by $(5\%Cr_2O_3: CoO)_T$ while it was 40.4%,
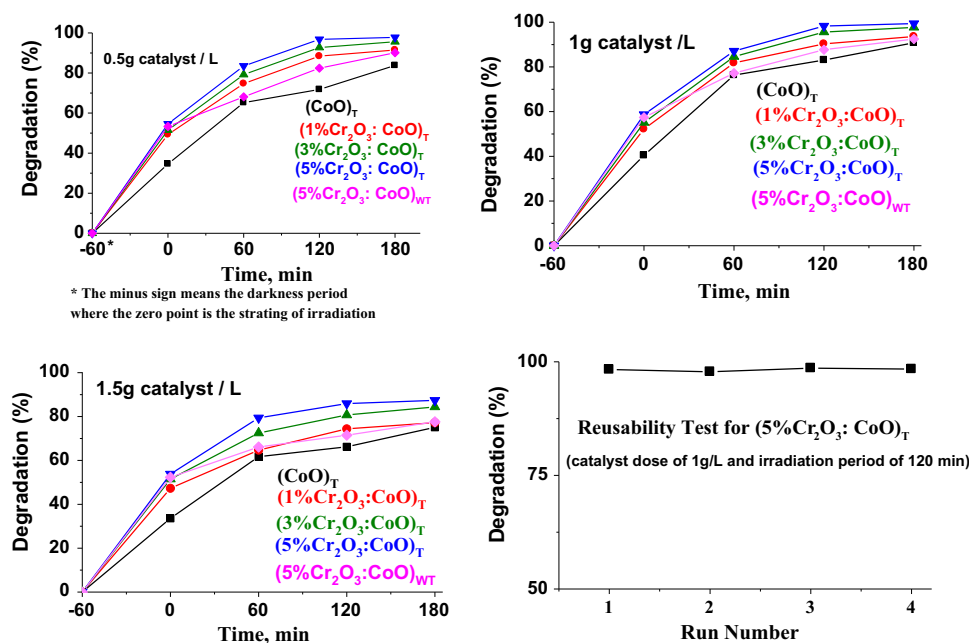
Fig. 8 The catalytic activity of as-prepared photocatalysts with different catalyst doses and reusability test for $(5\%Cr_2O_3: CoO)_T$

52.3%, 55,1%, and 57.4% for $(CoO)_T$, $(1\%Cr_2O_3: CoO)_T$, $(3\%Cr_2O_3: CoO)_T$, and $(5\%Cr_2O_3: CoO)_{WT}$, respectively. In the irradiation period, the optical properties (bandgap and PL intensity) and the textural structure determine the photocatalytic performance. The low E_g and PL intensity indicate low energy requirements to generate e−/h* pairs and the suppression of their radiative recombination process, leading to the enhancement of photon efficiency [26, 27]. On the other hand, the increase in surface area and pore dimensions increases the availability of the catalyst active sites and reduces the diffusional limitation of reactants and products [28]. As displayed in Table 2, and Fig. 7, all materials have absorption in the visible region with a difference in E_g value, PL intensity, and surface analysis. The strength of the influence of each of the three factors may vary, but the difference in the value of each of them determines which one is predominant. Although $(1\%Cr_2O_3: CoO)_T$ has the lowest PL intensity, it exhibits lower activity than $(3\%Cr_2O_3: CoO)_T$ and $(5\%Cr_2O_3: CoO)_T$, suggesting that a lower E_g value with an increase in the surface area of $(3\%Cr_2O_3: CoO)_T$ and $(5\%Cr_2O_3: CoO)_T$ is sufficient to be the predominant factor. For the same concept, $(5\%Cr_2O_3: CoO)_{WT}$ exhibits higher activity than $(CoO)_T$. On the contrary, the lower E_g value and higher surface area of $(5\%Cr_2O_3: CoO)_{WT}$ are not enough to compensate for the difference in PL intensity of $(1\%Cr_2O_3: CoO)_T$, which exhibits higher activity. According to these affecting factors, as displayed in Fig. 8, the catalytic activity increased in the order: $(CoO)_T$ < $(5\%Cr_2O_3: CoO)_{WT}$ < $(1\%Cr_2O_3: CoO)_T$ < $(3\%Cr_2O_3: CoO)_T$ < $(5\%Cr_2O_3: CoO)_T$.

The catalytic rate of the employed catalysts increased significantly upon increasing the catalyst dose from 0.5 to 1 g L^{-1} up to 120 min, where the degradation percentage reached 83.1%, 87.7%, 90.3, 95.6%, and 98.3% for $(CoO)_T$, $(5\%Cr_2O_3: CoO)_{WT}$, $(1\%Cr_2O_3: CoO)_T$, $(3\%Cr_2O_3: CoO)_T$ and $(5\%Cr_2O_3: CoO)_T$, respectively. These percentages were observed after 180 min of irradiation with the catalyst dose of 0.5 g L^{-1}. During the last hour of the irradiation period (between 120 and 180 min), a slight increase in pollutants disposal was observed, going from 98.3% to 99.4% for $(5\%Cr_2O_3: CoO)_T$. All catalysts showed damped activity when the catalyst dose was increased to 1.5 g L^{-1}. This might be explained by the fact that the excess catalyst dose of 1.5 g L^{-1} hinders light from penetrating the reaction medium [29].

3.3 Kinetics

The Eley–Rideal mechanism, which describes the reaction mechanism of an adsorbed reactant with another reactant in the gaseous phase, can be applied to the current reaction of photodegradation of organic pollutants by oxidation with O_2 over Cr-Co$_3$O$_4$ catalyst [30]. Irradiation of the photocatalyst results in electron–hole pair formation between valence and conduction bands in the photocatalyst. When a photoexcited electron reacts with oxygen, it forms a superoxide anion (O_2^-), which yields an OH radical when it is protonated. The positive hole also produces an OH radical in reaction with water, taking part in the degradation of pollutant molecules [31].
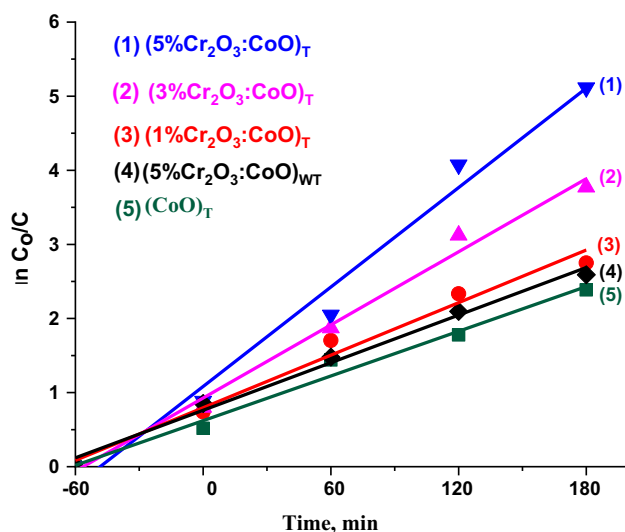
Fig. 9 Kinetic expression for the employed photocatalysts at the catalyst dose of 1 g L^{-1}

Eley–Rideal mechanism can be described by Eq. (6):

$$-\frac{dC}{dt} = K_r C \theta_{O_2} \qquad (6)$$

K_r = rate constant, C = concentration of the organic pollutants and θ_{O_2} = concentration of adsorbed oxygen.

Continuous aeration (at the ambient temperature, 32 °C) makes the reaction independent of the oxygen surface concentration. Hence, Eq. (6) devolves to Eq. (7), which changes to Eq. (8) on integration, where K_{ap} is the apparent or the observed rate constant and C_o is the initial concentration of the organic pollutants (150 ppm, TOC).

$$-\frac{dC}{dt} = K_{ap} C \qquad (7)$$

$$\ln \frac{C_o}{C} = K_{ap} t \qquad (8)$$

Figure 9 is obtained by applying Eq. (8) to the experimental data collected at a catalyst dose of 1 g L^{-1} (the detected optimal dose). The apparent rate constants (regression coefficients) of the as-prepared photocatalyst in descending order are given as follows: $0.98855 > 0.98711 > 0.97769 > 0.97531 \sim 0.97506$ min^{-1}, corresponding to $(3\%Cr_2O_3: CoO)_T$, $(5\%Cr_2O_3: CoO)_{WT}$, $(CoO)_T$, $(1\%Cr_2O_3: CoO)_T$ and $(5\% Cr_2O_3: CoO)_T$, respectively. Comparing these results with the textural analysis of the catalytic materials in Table 2 and the optical properties in Fig. 7, it becomes clear the important role of the textural structure. This is most probably linked with the bulky molecules of the organic contaminants, where the mass transfer through the pore system has a significant role [32].

3.4 Periodicity Test

The catalyst's potential for use in several cycles is the most crucial element in industrial applications. The reusability test for $(5\%Cr_2O_3: CoO)_T$, as a promised catalyst, was carried out under the optimal circumstances (catalyst dose of 1 g L^{-1} and irradiation time of 120 min), where any change in catalytic performance will be obvious. Figure 8 shows the stability of the catalyst throughout four successive cycles.

4 Conclusion

A series of Cr-doped cobalt oxide with different dopant concentrations were successfully prepared by simple and innovative swift procedures. PDA as a symmetric bidentate ligand exhibited good functionality in ordering the crystal lattice. The existence of Cr-dopant with the PDA causes a tuning of the textural structure. The main dopant effect is evident in the formation of surface oxygen vacancies, which induces sub-band levels between VB and CB, stabilizing the $e-/h^*$ pair and increasing photocatalytic activity. The study showed that the order–disorder in the lattice has a significant effect on the optical properties along with the dopant concentration. The catalytic performance of the employed catalysts in the disposal of different industrial organic pollutants confirmed all the results obtained from the various examinations of the catalytic materials. Among the prepared samples, $(5\%Cr_2O_3: CoO)_T$ exhibited the highest photoactivity with a disposal percentage of 99.4% after 180 min with a catalyst dose of 1.0 g L^{-1}. The kinetic study depicted the significant role of the pore dimensions due to the bulky molecules of the organic contaminants. The reusability test exhibited the stability of $(5\%Cr_2O_3: CoO)_T$ through four successive cycles.

Declarations

Conflict of interest The author declares that he has no known competing financial interests or personal relationships that could have appeared to influence the work reported in this paper.

References

1. Vinod, K.G.; Imran, A.; Tawfik, A.S.; Arunima, N.; Shilpi, A.: Chemical treatment technologies for waste-water recycling—an overview. RSC Adv. **2**, 6380–6388 (2012). https://doi.org/10.1039/c2ra20340e

2. Saravanan, R.; Gupta, V.K.; Narayanan, V.; Stephen, A.: Visible light degradation of textile effluent using novel catalyst ZnO/γ-Mn_2O_3. J Taiwan Inst Chem Eng **45**, 1910–1917 (2014). https://doi.org/10.1016/j.jtice.2013.12.021

3. Mya, M.K.; Nair, A.S.; Jagadeesh, V.B.; Rajendiran, M.; Seeram, R.: A review on nanomaterials for environmental remediation. Energy Environ. Sci. **5**, 8075–8109 (2012). https://doi.org/10.1039/c2ee21818f

4. World Health Organization. Global health observatory data repository. WHO: (2008) http://apps.who.int/ghodata/?vid=10012#

5. Muhammad, S.; Majid, M.; Nida, M.; Mohsin, S.; Nadia, A.; Muhammad, H.: Ag-Co_3O_4: synthesis, characterization and evaluation of its photocatalytic activity towards degradation of rhodamine B dye in aqueous medium. Chin. J. Chem. Eng. **26**, 1264–1269 (2018). https://doi.org/10.1016/j.cjche.2018.02.024

6. Meng, N.C.; Bo, J.; Christopher, W.K.C.; Chris, S.: Recent developments in photocatalytic water treatment technology: a review. Water Res. **44**, 2997–3027 (2010). https://doi.org/10.1016/j.watres.2010.02.039

7. Jeevitha, R.R.; Kandasamy, P.: Sunlight-induced photocatalytic degradation of organic pollutants by carbon-modified nanotitania with vegetable oil as precursor. Ind. Eng. Chem. Res. **50**, 3130–3138 (2011). https://doi.org/10.1021/ie101259p

8. Nasser, H.S.; Mohamed, A.S.: Stover ash—extracted mixed oxides surface-doped with Ni for photo-degradation of water organic pollutants. J. Environ. Anal. Chem. (2021). https://doi.org/10.1080/03067319.2021.2000601

9. Ciara, B.; Gokulakrishnan, S.; Suresh, C.P.: Recent advances in photocatalysis for environmental applications. J. Environ. Chem. Eng. **6**, 3531–3555 (2018). https://doi.org/10.1016/j.jece.2017.07.080

10. Kerli, S.: Boron-doped cobalt oxide thin films and its electrochemical properties. Mod. Phys. Lett. B **30**, 1650343–1650350 (2016). https://doi.org/10.1142/S0217984916503437

11. Vannier, V.; Schenk, M.; Katharina, K.-H.; Bahlawane, N.: Preparation and characterisation of chromium-doped cobalt oxide spinel thin films. J. Mater. Sci. **47**, 1348–1353 (2012). https://doi.org/10.1007/s10853-011-5909-6

12. Deepa, G.; Sunil, K.; Jonghyun, C.; Romakanta, B.; Tej, P.P.; Ram, K.G.; Xiao, S.; Sanjay, R.M.: Electrochemical performance of iron-doped cobalt oxide hierarchical nanostructure. Processes **9**, 2176–2197 (2021). https://doi.org/10.3390/pr9122176

13. Faisal, A.; Khalid, N.R.: Facile synthesis and properties of chromium-doped cobalt oxide (Cr-doped Co_3O_4) nanostructures for supercapacitor applications. Appl. Nanosci. **10**, 1481–1488 (2020). https://doi.org/10.1007/s13204-020-01266-5

14. Yang, H.; Keyu, T.; Huamei, D.; Li, L.; Yun, G.: Cr-doped (Co, Ni)$_3$S$_4$/Co$_9$S$_8$/Ni$_3$S$_2$ nanowires/nanoparticles grown on Ni foam for hybrid supercapacitor. J. Alloys Compd. **835**, 155254 (2020). https://doi.org/10.1016/j.jallcom.2020.155254

15. Hitkari, G.; Sandhya, S.; Gajanan, P.; Shrivash, M.K.; Deepak, K.: Synthesis of chromium doped cobalt oxide (Cr:Co_3O_4) nanoparticles by co-precipitation method and enhanced photocatalytic properties in the visible region. J. Mater. Sci. Eng. **7**, 419–424 (2018). https://doi.org/10.4172/2169-0022.1000419

16. Oxtoby, D.W.; Gillis, H.P.; Butler, L.J.: Principles of Modern Chemistry, 8th edn. Cengage Learning, Boston (2016)

17. Cullity, B.D.; Stock, S.R.: Elements of X-ray Diffraction, 3rd edn. Pearson Education Limited, London (2014)

18. Dana, G.; Ioana, M.; Daniela, C.C.; Luminita, P.; Jose, M.C.-M.; Petre, O.; Silviu, P.; Ovidiu, O.; Viorica, P.; Valentin, T.; James, P.S.W.: Structural, magnetic and catalytic properties of cobalt chromite obtained through precursor method. Mater. Res. Bull. **62**, 52–64 (2015). https://doi.org/10.1016/j.materresbull.2014.11.009

19. Mark, C.B.; Brad, P.P.; Andrew, P.G.; Leo, W.M.L.; Andrea, R.G.; Roger, S.C.S.: Resolving surface chemical states in XPS analysis of first row transition metals, oxides and hydroxides: Cr, Mn, Fe, Co and Ni. Appl. Surf. Sci. **257**, 2717–2730 (2011). https://doi.org/10.1016/j.apsusc.2010.10.051

20. Paul, S.B.; Eugene, S.I.; Connie, J.N.: The interpretation of XPS spectra: Insights into materials properties. Surf. Sci. Rep. **68**, 273–304 (2013). https://doi.org/10.1016/j.surfrep.2013.03.001

21. Orliukas, A.F.; Šalkus, T.; Kežionis, A.; Venckutė, V.; Kazlauskienė, V.; Miškinis, J.; Laukaitis, G.; Dudonis, J.: XPS and impedance spectroscopy of some oxygen vacancy conducting solid electrolyte ceramics. Solid State Ion. **188**, 36–40 (2011). https://doi.org/10.1016/j.ssi.2010.11.001

22. Salah, A.H.; Ahmed, M.A.-S.; Nasser, H.S.; Samia, A.H.; Hamdi, A.H.: Catalytic performance of organically templated nano nickel incorporated-rice husk silica in hydroconversion of cyclohexene and dehydrogenation of ethanol. Egypt. J. Pet. **22**, 179–188 (2013). https://doi.org/10.1016/j.ejpe.2012.09.009

23. Gouveia, A.F.; Sczancoski, J.C.; Ferrer, M.M.; Lima, A.S.; Santos, M.R.M.C.; Li, M.S.; Santos, R.S.; Longo, E.; Cavalcante, L.S.: Experimental and theoretical investigations of electronic structure and photoluminescence properties of β-Ag_2MoO_4 microcrystals. Inorg. Chem. **53**, 5589–5599 (2014). https://doi.org/10.1021/ic500335x

24. Asha, K.; Thadathil, S.S.; Eoin, M.; Swapankumar, G.: One-pot synthesis of ultra-small cerium oxide nanodots exhibiting multicolored fluorescence. J. Colloid Interface Sci. **389**, 16–22 (2013). https://doi.org/10.1016/j.jcis.2012.09.009

25. Asha, K.; Thadathil, S.S.; Mohamed, A.P.; Unnikrishnan, S.H.; Swapankumar, G.: Concentration quenching in cerium oxide dispersions via a Förster resonance energy transfer mechanism facilitates the identification of fatty acids. RSC Adv. **5**, 23965–23972 (2015). https://doi.org/10.1039/C4RA17326K

26. Liqiang, J.; Baifu, X.; Fulong, Y.; Lianpeng, X.; Baiqi, W.; Honggang, F.: Effects of surface oxygen vacancies on photophysical and photochemical processes of Zn-doped TiO_2 nanoparticles and their relationships. J. Phys. Chem. B **110**, 17860–17865 (2006). https://doi.org/10.1021/jp063148z

27. Raji, A.; Thomas, N.J.I.E.; Suguna, P.; Dhanapalan, K.; Yong, R.L.: Effective photocatalytic degradation of anthropogenic dyes using graphene oxide grafting titanium dioxide nanoparticles under UV-light irradiation. J. Photochem. Photobiol. A **333**, 92–104 (2017). https://doi.org/10.1016/j.jphotochem.2016.10.021

28. Hansheng, L.; Jungang, W.; Congbiao, C.; Litao, J.; Bo, H.; Debao, L.: Effects of macropores on reducing internal diffusion limitations in Fischer–Tropsch synthesis using a hierarchical cobalt catalyst. RSC Adv. **7**, 9436–9445 (2017). https://doi.org/10.1039/C6RA27166A

29. Emam, E.A.; Aboul-Gheit, N.A.K.: Photocatalytic degradation of oil-emulsion in water/seawater using titanium dioxide. Energy Sources A Recov. Util. Environ. Effects **36**, 1123–1133 (2014). https://doi.org/10.1080/15567036.2010.544154

30. Huancong, S.; Min, H.; Yuandong, H.; Lifeng, C.; Linna, Z.; Mingqi, C.; Linhua, J.; Hussameldin, I.; Paitoon, T.: Eley–Rideal model of heterogeneous catalytic carbamate formation based on CO_2-MEA absorptions with CaCO. R. Soc. Open Sci. **6**, 190311 (2019). https://doi.org/10.1098/rsos.190311

31. Palominos, R.; Freer, J.; Mondaca, M.A.; Mansilla, H.D.: Evidence for hole participation during the photocatalytic oxidation of the antibiotic flumequine. J. Photochem. Photobiol. A **193**, 139–145 (2008). https://doi.org/10.1016/j.jphotochem.2007.06.017

32. Ryoji, T.; Satoshi, S.; Toshiaki, S.; Hideyo, N.: Effect of pore size on the liquid-phase pore diffusion of nickel nitrate. Phys. Chem. Chem. Phys. **4**, 3800–3805 (2002). https://doi.org/10.1039/b202024f